ACS APPLIED MATERIALS & INTERFACES

Research Article

www.acsami.org

Controlling the Morphology of Organic Crystals with Filamentous Bacteriophages

Whirang Cho,[†] Xiaomeng Liu,[‡] James Forrest,[‡] Jeffrey D. Fowler,[‡] and Eric M. Furst*[,†]

[†]Department of Chemical and Biomolecular Engineering and Center for Molecular and Engineering Thermodynamics, University of Delaware, 150 Academy Street, Newark, Delaware 19716, United States

[‡]Syngenta Crop Protection 410 Swing Road, Greensboro, North Carolina 27409, United States

Supporting Information

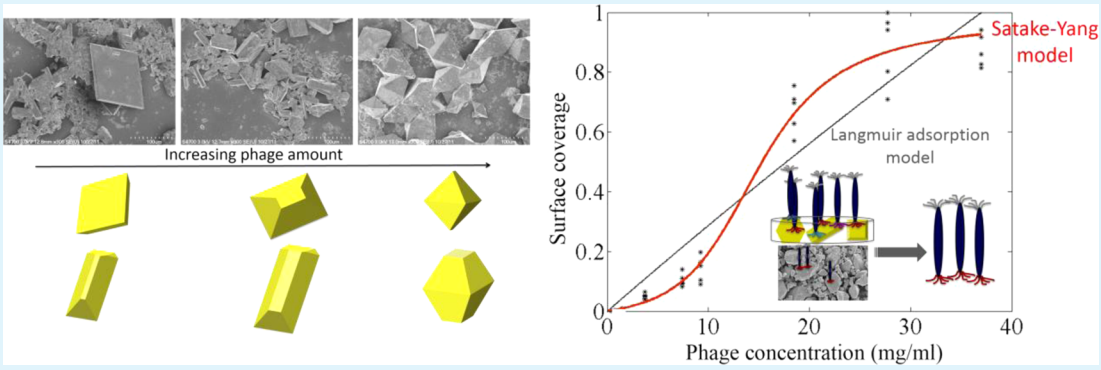

ABSTRACT: The preparation of thiamethoxam (TMX) organic crystals with high morphological uniformity was achieved by controlled aggregation-driven crystallization of primitive TMX crystals and phage using the filamentous M13 bacteriophage. The development of a regular, micrometer-sized, tetragonal-bipyramidal crystal structure was dependent on the amount of phage present. The phage appears to affect the supersaturation driving force for crystallization. The phage adsorption isotherm to TMX was well-fitted by the Satake−Yang model, which suggests a cooperative binding between neighboring phages as well as a binding of phage with the TMX crystal surface. This study shows the potential of phage additives to control the morphology and morphological uniformity of organic crystals.

KEYWORDS: *M13 bacteriophage, bioinspired crystallization, thiamethoxam (TMX) organic crystals, Satake−Yang model adsorption isotherm, biointerfaces*

1. INTRODUCTION

Understanding and controlling crystallization with the goal of efficiently producing particles with specific size distribution, morphology, and structure (crystalline polymorph and degree of crystallinity) is a critical need in many industries.[1−3] Controlling the shape and size of crystalline solids is important for their manufacturing and use in a range of applications, including in the production of fine chemicals, pharmaceuticals, and foods, in drug delivery and release, and for technologies as diverse as bio/photocatalysis, thin-film solar cells, and antibacterial fabrics.[4−14] Crystallization involves the formation of a new phase (nucleation) and the growth of that phase (crystal growth), of which precise tuning is intimately linked with the resulting crystal structures.[15−18]

Control of the crystal size is usually achieved by manipulating the rate of nucleation and crystal growth, whereas the crystal morphologies can be manipulated by altering the relative growth rates of crystal faces.[19] Crystal morphologies, in particular, have a strong influence on downstream processes, such as filtration, washing, drying, and packaging, in addition to storage and handling, as well as their final applications, including the bioavailability of pharmaceuticals or reactivity of catalysts.[11,20−22] Different polymorphs of organic compounds may have distinct crystal habits.[13,23] Clearly, the ability to engineer organic crystalline solids with the desired size, morphology, and structure is important for the synthesis of high-quality materials with defined surface and bulk properties, especially for improved bioavailability and sustainability of an active pharmaceutical ingredient (API).[17,18]

Biomimetic strategies for manipulating crystalline solids have recently drawn keen attention. Biological organisms direct the growth of biominerals such as bones, teeth, and seashells.[24,25] Several previous studies demonstrated that biomolecules, such as peptides and enzyme-mimicking molecular assemblies, effectively direct the assembly of inorganic nanoparticles with controlled compositions and nanostructures because of their unique sequence-specific self-assembly and their substrate recognition properties.[26−34] In particular, the filamentous

Received: October 22, 2014
Accepted: July 8, 2015
Published: July 8, 2015

DOI: 10.1021/acsami.5b05548
ACS Appl. Mater. Interfaces 2015, 7, 15707−15715

Scheme 1. Schematic Illustration of the Coprecipitation of a TMX Supersaturated Solution with Bacteriophage

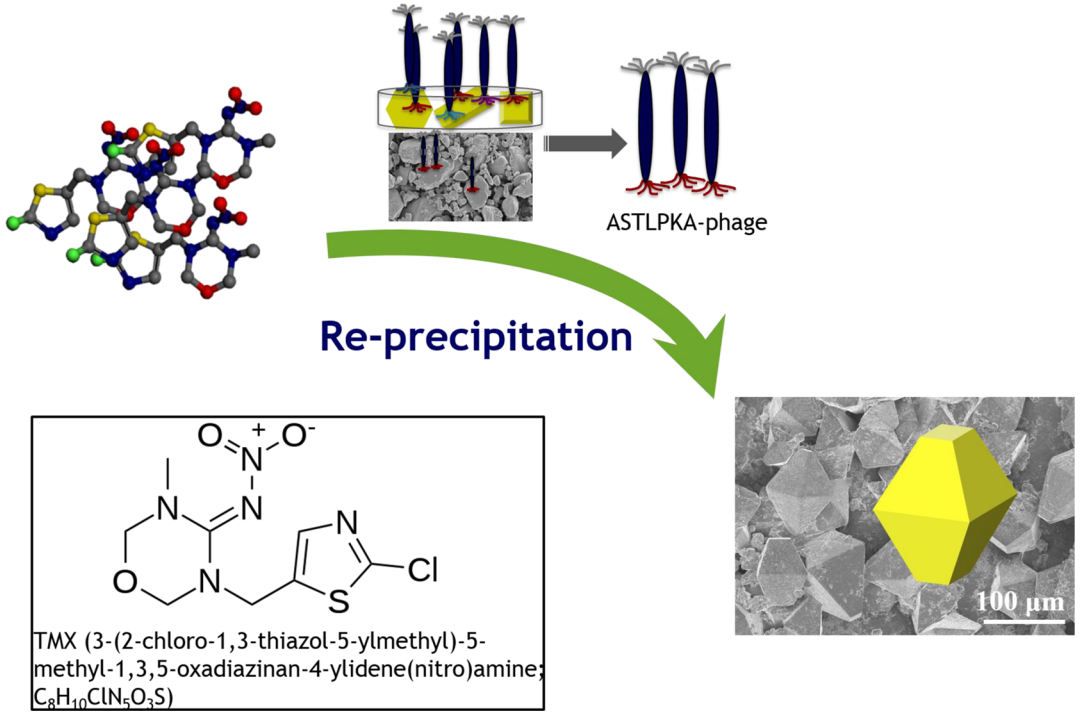

M13 bacteriophage has demonstrated exciting properties such as self-assembly,[35] nanoparticle nucleation,[36−38] catalysis,[39,40] and the formation of complex 2D or 3D microstructures.[41−43]

In the present study, we describe the shape of organic crystals of thiamethoxam [TMX; 3-(2-chloro-1,3-thiazol-5-ylmethyl)-5-methyl-1,3,5-oxadiazinan-4-ylidene(nitro)amine; $C_8H_{10}ClN_5O_3S$][44] during controlled aggregation-driven crystallization[33,45] in the presence of M13 bacteriophage (Scheme 1). TMX is used as a model compound of organic crystalline materials, specifically APIs. Controlled crystallization of APIs such as TMX is challenging in view of their various chemical structures[18] and complex microstructures involving different facets and defects.[46] For example, well-defined TMX crystals are difficult to grow mainly because of its relatively high water solubility (4.1 g/L at 25 °C), which leads to uncontrolled aggregation when precipitated from an aqueous solution (see Figure S1 in the Supporting Information, SI).

Using phage display screening against a combinatorial library, we previously identified several phages that exhibit at least 1000 times the binding affinity of wild-type M13. These phages express heptapeptide sequences that are rich in hydrophobic, hydrogen-bonding amino acids and proline. Among the peptide sequences identified, M13 displaying the pIII domain heptapeptide ASTLPKA exhibits the strongest binding to TMX in competitive binding assays.[46] In this study, we focus on ASTLPKA and a wild-type M13KE phage to investigate their effects on the controlled crystallization of TMX. We demonstrate that TMX crystal structures with high morphological uniformity can be controllably formed in the presence of phages. We show that the concentration of the phage affects the supersaturation level upon cooling. Phage additives affect the formation of TMX crystals with well-defined morphology after a critical concentration is reached. We further demonstrate that the adsorption isotherm of phage on a TMX crystalline solid in the solution environment is well-fitted by a Satake−Yang model adsorption isotherm, which suggests that cooperative phage−phage interactions as well as phage−surface binding occur.[47−49] We hypothesize that such cooperative binding (phage−phage self-association) and binding of M13 bacteriophage to solid surfaces (phage−TMX complex) could lead to favorable effects through the targeted manipulation of surface chemistry in complex mixtures of colloidal suspensions.

2. EXPERIMENTAL SECTION

2.1. Materials. A commercial phage library (Ph.D.-7, New England Biolabs, Ipswich, MA) was used in these studies. Poly(ethylene glycol) (M_w = 8000 g/mol), Tris-HCl, glycine-HCl (Trizma hydrochloride, T6666), NaCl (BioReagent ≥99.5%, S5886), sodium iodide (ACS reagent ≥99.5%, 383112), Tween-20 (P9416), and ethanol (ACS reagent ≥99.5%, 459844) were purchased from Sigma-Aldrich (St. Louis, MO) and used without further purification. 5-Bromo-4-chloro-3-indolyl-β-D-galactopyranoside (X-gal, AC327241000) was obtained from Acros Organics (Morris Plains, NJ). Isopropyl-β-D-thiogalactopyranoside (IPTG, BP1755) and bovine serum albumin (BSA, BP1600) were purchased from Fisher Scientific (Pittsburgh, PA). TMX air-milled to less than 10 μm diameter (95th percentile by volume) was provided by Syngenta Crop Protection (Greensboro, NC). The molecular structure of TMX is as shown in Scheme 1.

2.2. Phage Display Screening for the Selection of TMX Binding Peptide Motifs. Combinatorial phage display libraries with randomized 7-mer peptides displayed on M13 bacteriophage from the N-terminus of the pIII capsid proteins (Ph.D.-7, New England Biolabs, Ipswich, MA) were used to identify peptide sequences with selective and specific binding affinity to TMX organic crystals, as described in our previous study.[46] Briefly, the initial phage library solution was diluted by adding 10 μL of library [~1 × 10^{13} plaque forming units (pfu)/mL] to 1 mL of 0.1% TBST buffer (50 mM Tris-HCl of pH 7.5, 150 mM NaCl, and 0.1% v/v Tween-20). A total of 100 μL of the diluted phage library was then introduced into the TMX suspension and incubated at room temperature for 1 h with gentle rocking. The sample was then washed several times with a TMX-saturated 0.1% TBST buffer and transferred into a new centrifuge tube. This step removed nonspecific binding phage or any phage with a strong affinity to the polypropylene centrifuge tubes. Next, to measure the number of phages adsorbed to TMX, phages were eluted from the TMX surface

DOI: 10.1021/acsami.5b05548
ACS Appl. Mater. Interfaces 2015, 7, 15707−15715

by incubating with 100 μL of a 0.2 M glycine-HCl (pH 2.2) and 1 mg/mL BSA solution, which was then neutralized with 15 μL of 1 M Tris base (pH 9.0). The eluted phages were amplified with 20 mL of a 1:100 diluted overnight culture of *Escherichia coli* (ER 2738) that was grown in LB media at 37 °C for 4.5 h and purified through poly(ethylene glycol) precipitation. These panning procedures were repeated three times, using increasing Tween-20 concentration in each round (0.1, 0.3, and 0.5% v/v) to increase the stringency of binding to the TMX target. Elution demonstrates that the phages may be removed from the crystal surfaces.

2.3. TMX Crystallization in the Presence of Phage. TMX-binding phage displaying heptapeptide ASTLPKA was amplified in a 1:100 diluted overnight culture of *E. coli* (ER 2738) in 1 L of autoclaved LB media at 37 °C and purified through $^1/_6$ volume of 20% poly(ethylene glycol) precipitation/2.5 M NaCl. We performed the amplification of ASTLPK−peptides expressing phage in a large scale (1 L of LB culture, 6 times) that produced hundreds of milligrams of phage. The phage concentration was quantified by dry weight. After repeated centrifugation and redispersion steps, the spun-down phage pellet was resuspended at varying concentrations (e.g., 37, 3.7, and 0.37 mg/mL) in a TBS solution. 500 μL of an aqueous slurry containing 1.1 wt % TMX in a TBS solution was placed in a 1.5 mL microcentrifuge tube and was then heated to 50 °C to ensure the complete dissolution of the TMX solute. Solutions were removed from the heating bath, and 250 μL of an ASTLPKA bacteriophage suspended solution with at the above concentrations was added to each microcentrifuge tube. They were then cooled and incubated at room temperature for at least 1day while being monitored for the onset time of precipitation (see Figure S2 in the SI). The precipitation was carried out with and without the presence of ASTLPKA bacteriophage suspended in a TBS solution. Comparisons were made with the crystals precipitated in the presence of either a TMX-saturated solution or a wild-type M13KE phage at the same concentration (37 mg/mL). To see the effect of different aging conditions on the size of the TMX crystals, samples were incubated in the fridge or in a hot bath with decreasing temperature controlled at a rate of −5 °C/4 h. The shapes of the wet crystals were observed by optical microscopy using square capillary tubes. The morphology of the resulting TMX precipitate was characterized by field-emission scanning electron microscopy (FE-SEM) on a JSM 7400F at a 5 kV accelerating voltage. TMX precipitate samples were placed on SEM stubs with a carbon tape after removal of the supernatant (unbound phage solution). The stubs were rinsed with water and completely air-dried in a fume hood for approximately 2−3 h. To prevent electron charging, gold was sputtered on the samples. Graphical data were displayed as mean and standard deviations, and the Student *t* test was used for statistical analyses.

2.4. Theoretical Background (Satake−Yang Model). We adapt an analytical expression for the theoretical phage-binding isotherm curve using the Satake−Yang cooperative surfactant/polyelectrolyte adsorption model. This fitting method provides estimates of the Satake−Yang binding parameters by a least-squares fitting of the experimental data to the theoretical phage-binding isotherm.[47] The model was originally derived based on the assumption that each polyelectrolyte is regarded as a 1D lattice with N sites onto which the oppositely charged surfactant can adsorb.[47−49] There are two types of adsorption sites in this model: cooperative binding, where the neighboring site is occupied by another surfactant, and noncooperative adsorption, where the adjacent site is vacant.[50] The average site coverage, θ, is the ratio of the occupied sites to all possible binding sites. By interpretation of the average coverage θ in terms of experimentally measurable quantities, such as the free surfactant concentration (C_s), the binding isotherm is[48−50]

$$\theta = \frac{1}{2}\left[1 + \frac{KuC_s - 1}{\sqrt{(1 - KuC_s)^2 + \frac{4KuC_s}{u}}}\right]$$

The binding parameter Ku characterizes the binding strength, and the adsorption cooperativity u quantifies the favorability of cooperative binding. They can be estimated directly from the binding isotherm when the fractional coverage is equal to a half using the following expressions:[47,49,51−53]

$$Ku = \frac{1}{C_s(\theta = 0.5)}$$

$$u = 16\left(\frac{d\theta}{d \ln C_s}\right)_{\theta=0.5}$$

To measure the number of phages bound to TMX, a binding assay[54] was carried out against 200 μL of TMX in a TBS buffer using 100 μL of phages with varied concentrations (0.37, 0.74, 1.48, 3.7, 7.4, 9.25, 18.5, 27.75, and 37 mg/mL). After one washing step, the bound phages were eluted from TMX by 0.2 M glycine-HCl (pH 2.2) and a 1 mg/mL BSA solution, which was then neutralized with 1 M Tris base (pH 9.0). The bound phages were quantified by the titration method described above (see section 2.2). All measurements were performed 4−6 times for each concentration of phage to confirm repeatability, and the curves were normalized to the maximum value of bound phage. The optimal fitting parameters (Ku and u) were obtained by minimizing the sum of the squared error between the measured data points and data estimated from the Satake−Yang model.

3. RESULTS AND DISCUSSION

3.1. Crystal Morphology. Following the crystallization procedure outlined in section 2.3, crystallization was carried out with and without ASTLPKA phage. First, a 1.1 wt % TMX-suspended solution was heated to dissolve the TMX solute, as shown in Figure 1 (position a) along with the empirical

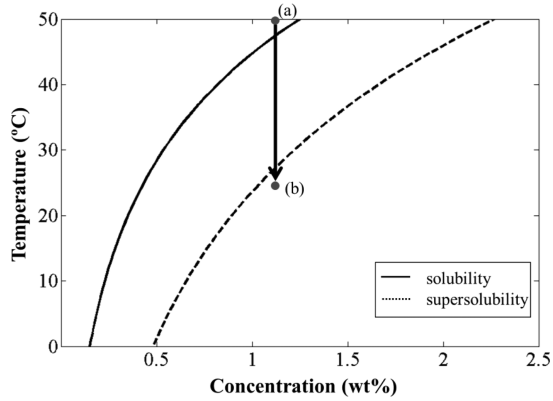

Figure 1. Solubility of TMX in water depending on the temperature and metastable zone boundary. (a) Starting point: a supersaturated 1.1 wt % TMX-suspended solution. (b) Reprecipitation point: cooling to room temperature.

solubility curve and metastable zone boundaries. Crystallization was induced by cooling a supersaturated TMX solution to room temperature with or without ASTLPKA bacteriophage suspended in a TBS solution (position b). The onset time of precipitation was observed to change depending on the ratio between the amount of phage and the TMX suspended solution ($\chi = W_{phage}/W_{TMX}$). When a supersaturated TMX solution (supersaturation level: 2.7) and phage were mixed, fine particles were formed after a period of time, as summarized in Table 1. All of the induction times (defined as the elapsed time between the starting point of cooling and the detection of the first TMX crystals) of a phage−TMX-containing solution were shorter than the 560 ± 14.6 s observed when the same amount of a phage-free TBS solution was added to the TMX solution. The induction time became shorter as the phage concentration

DOI: 10.1021/acsami.5b05548
ACS Appl. Mater. Interfaces 2015, 7, 15707−15715

Table 1. Comparison of the Elapsed Time before the Precipitation Was Initiated, Obtained by Heating to 50 °C, and Then Aged at Room Temperature in the Presence of M13 Bacteriophage Expressing TMX-Binding ASTLPKA with Varied Concentrations[a]

sample	induction time (s)
χ = 3.4	308 ± 17.0
χ = 0.34	390 ± 14.1
χ = 0.03	455 ± 7.1
no phage	560 ± 14.6

[a]Here, $\chi = W_{phage}/W_{TMX}$ (the weight ratio of ASTLPKA bacteriophage to TMX).

increased. The consequent metastable supersaturation time thus becomes smaller with increasing phage concentration, which could result in different levels of supersaturation in the presence of phage.

After sufficient time (~1 day) was allowed to complete the crystallization of TMX, the crystal morphology was characterized by FE-SEM (Figure 2). In the presence of ASTLPKA phage (37 mg/mL), TMX formed predominantly uniform and well-defined tetragonal-bipyramidal-shaped crystals. Figure 2a shows the bipyramidal shapes with a typical width (r_W) of approximately 60 μm and a length (r_L) of approximately 100 μm. The Miller index of bipyramidal TMX could be assigned as the inverse intercepts of the face along the crystallographic axes based on geometrical analysis (see Figure S3 in the SI). These TMX crystals were generally distinct from each other and not fused together, although this aspect was not quantified.

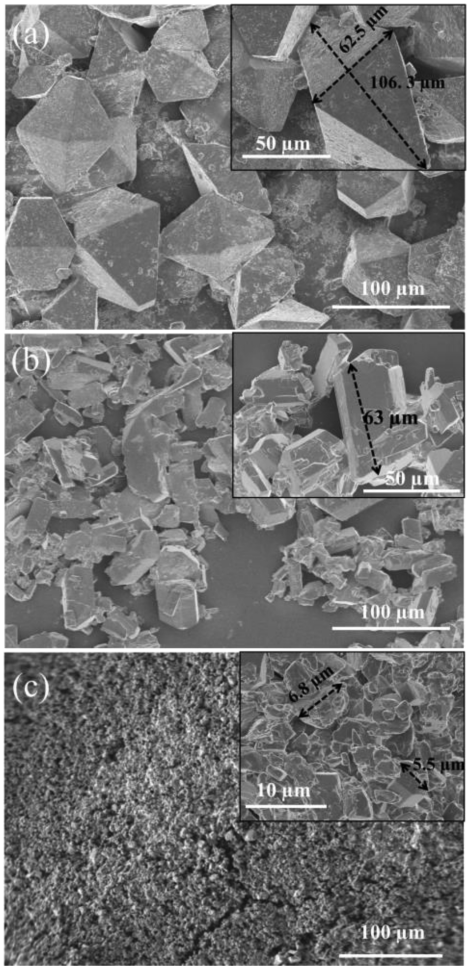

Figure 2. FE-SEM images of the TMX crystals: (a) having tetragonal-bipyramidal form obtained by aging the supersaturated TMX solution (heated up to 50 °C) in the presence of M13 bacteriophage expressing TMX-binding ASTLPKA; (b) obtained by adding the TBS solution (without phage); (c) obtained by adding the TBS solution (without a supersaturation step). Insets: magnified views.

An SEM image of crystals precipitated in the absence of ASTLPKA phage is represented in Figure 2b. In this case, the crystal shape was not homogeneous and no tetragonal-bipyramidal particles were observed. On the other hand, adding a phage-free TBS solution without heating gave rise to relatively small and aggregated crystals (native TMX), as represented in Figure 2c. We noted that during reprecipitation from a saturated solution, the size of the TMX crystals increased by a process of nucleation of small TMX crystal clusters, followed by association of these small TMX particles into the larger microstructure.

Further comparison was made with the TMX crystals coprecipitated with a TMX-saturated (37 mg/mL) solution under the same experimental conditions. The precipitation started as soon as a TMX-saturated solution was added to the supersaturated TMX solution. Interestingly, it showed rather smaller irregular aggregates, similar to native TMX (see Figure S4 in the SI). These observations suggest that the growth of TMX microcrystals with well-defined bipyramidal morphology is facilitated by phage additives through a process of the cooperative attachment of small neighboring TMX crystalline particles, while preventing the undesired nucleation of seeds.[55,56]

Figure 3 shows FE-SEM images of TMX crystals and the corresponding crystal shape distributions obtained by different aging conditions in the presence of a constant amount of ASTLPKA phage (37 mg/mL). The resulting TMX crystals are of tetragonal-bipyramidal shape and can be characterized by the ratio between the side of the truncation facets (a) and the side of the bipyramid (b).[13] The value of b is 40.1 ± 11.4 μm, and the a/b ratio is 0.24 ± 0.15 when a supersaturated TMX solution was aged at room temperature (Figure 3a). TMX crystals obtained from the precipitates following a rapid cooling trajectory while being incubated in a fridge had a smaller size (b = 33.0 ± 9.7 μm) compared with TMX crystals grown under room temperature (see Figure 3b). This value is about 18% smaller (the difference is statistically significant) than that of TMX crystals prepared at room temperature, while no significant difference in the a/b ratio was observed (see Figure 4). On the other hand, TMX crystals prepared by decreasing the aging temperature in a stepwise fashion, 50 °C to room temperature at a rate of −5 °C/4 h, had a statistically significantly different bipyramidal size (b = 229.3 ± 63.3 μm) as well as a larger size ratio (a/b = 0.64 ± 0.10), as shown in Figures 3c and 4. These data revealed that the sizes and aspect ratios of TMX bipyramidal crystals could be controlled by differing aging conditions and corresponding supersaturation levels, which affects the precipitation and clustering rate of TMX molecules.[22]

Samples were also prepared using a wild-type M13KE phage. Our previous research demonstrated that TMX-binding phage expressing the ASTLPKA heptapeptide exhibits an approximately 8-fold higher unbinding force compared to that of wild-type M13KE.[46] However, there was no significant difference in the precipitation time compared with that of ASTLPKA

DOI: 10.1021/acsami.5b05548
ACS Appl. Mater. Interfaces 2015, 7, 15707−15715

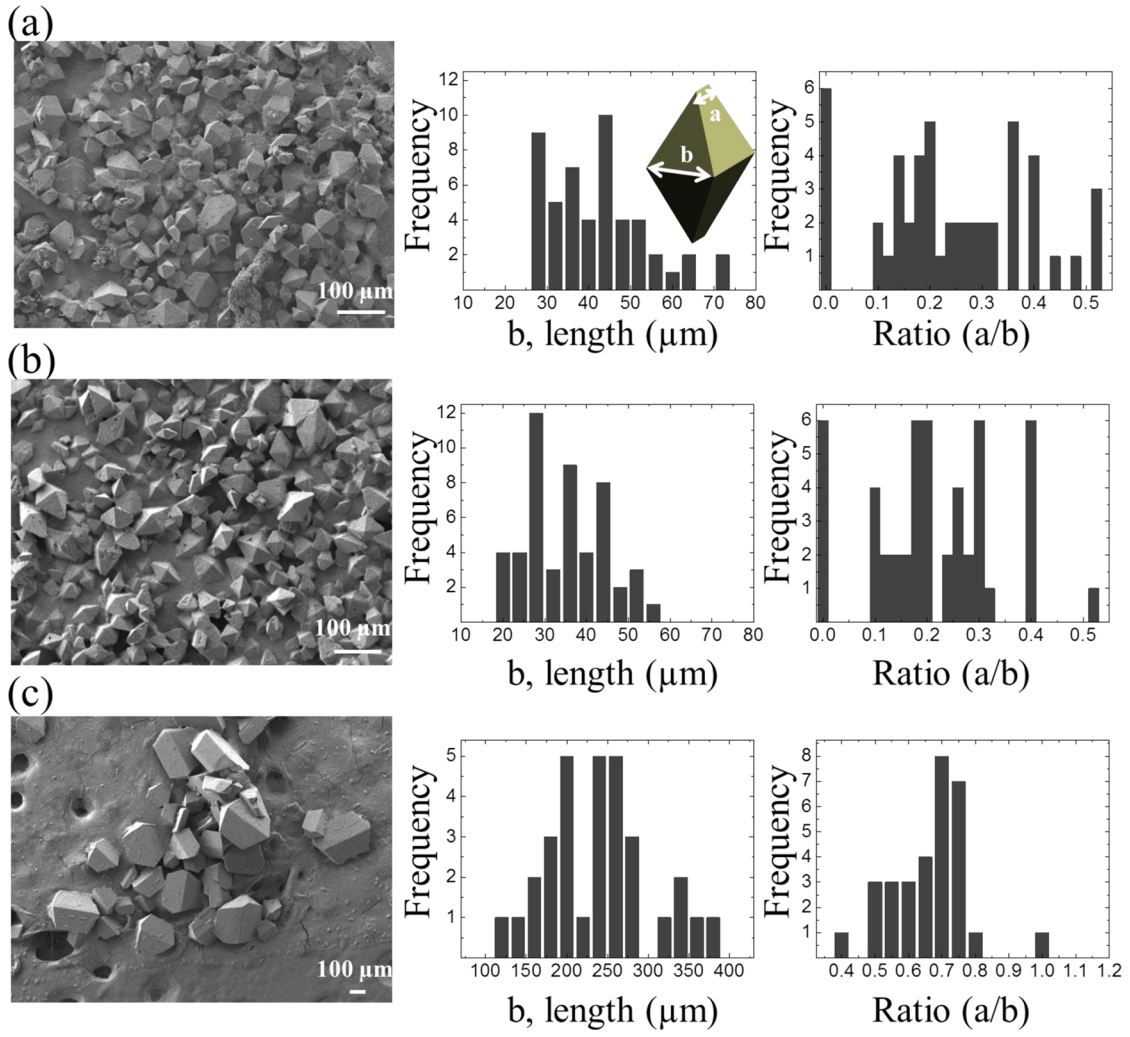

Figure 3. FE-SEM images of morphologies and corresponding size and shape distribution of the tetragonal bipyramidal TMX crystals obtained in the presence of M13 bacteriophage expressing TMX-binding ASTLPKA [W_{phage}/W_{TMX} (χ) = 3.4] with different aging conditions: (a) incubated at room temperature; (b) incubated in a fridge (4 °C); (c) stepwise cooling to room temperature [−5 °C/4 h; n(RT), n(refrigeration) = 50; n(slow crystallization) = 30].

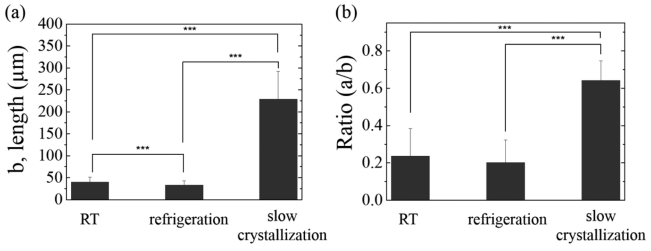

Figure 4. Effect of the different aging conditions on the tetragonal-bipyramidal shape of TMX crystals: (a) length of the bipyramid side; (b) the ratio of the truncation facets and the side of the bipyramid (Student t test; ***, $p < 0.001$).

displayed phage. Wild-type phage also affected crystallization and led to regular crystal morphologies under the same experimental conditions as those for ASTLPKA phage. Although both ASTLPKA-displaying and M13KE phages formed bipyramidal crystals, the latter crystals had distinctly different aspect ratios of length, r_L, to width, r_w (Figure 5c,d). TMX crystals grown with ASTLPKA bacteriophage had a higher aspect ratio (∼2), whereas wild-type M13KE bacteriophage produced a truncated tetragonal bipyramid having pronounced top truncation facets (aspect ratio ∼1). These data suggest that the formation of microsized TMX bipyramidal crystals depends upon the collective characteristics of phage particles and consequent effect on the supersaturation pathways in the course of coprecipitation of phage and TMX. In addition, it might be related to the favorable orientations of adsorbed phage at crystal surfaces.

To investigate the effect of the ratio between the amount of phage and the TMX suspended solution (χ) on the TMX crystal shape, the concentration of phage was varied from 37, 3.7, and 0.34 mg/mL, while the concentration of TMX was fixed at 11 mg/mL. When χ is 3.4, TMX crystalline particles grew into well-developed tetragonal-bipyramidal shapes, as shown in Figure 6d. Crystals obtained with smaller values of χ (i.e., 0.34) had a lower fraction of bipyramidal shapes and were more abundant in the elongated tetragonal prism shapes (Figure 6c). Moreover, as χ decreased to 0.03 (Figure 6b), TMX nuclei flocculated into the aggregates of smaller elongated tetragonal prisms. On the other hand, TMX crystals precipitated without phage had nonhomogeneous and complex shapes with different facets and defects, as shown in Figure 6a.

DOI: 10.1021/acsami.5b05548
ACS Appl. Mater. Interfaces 2015, 7, 15707−15715

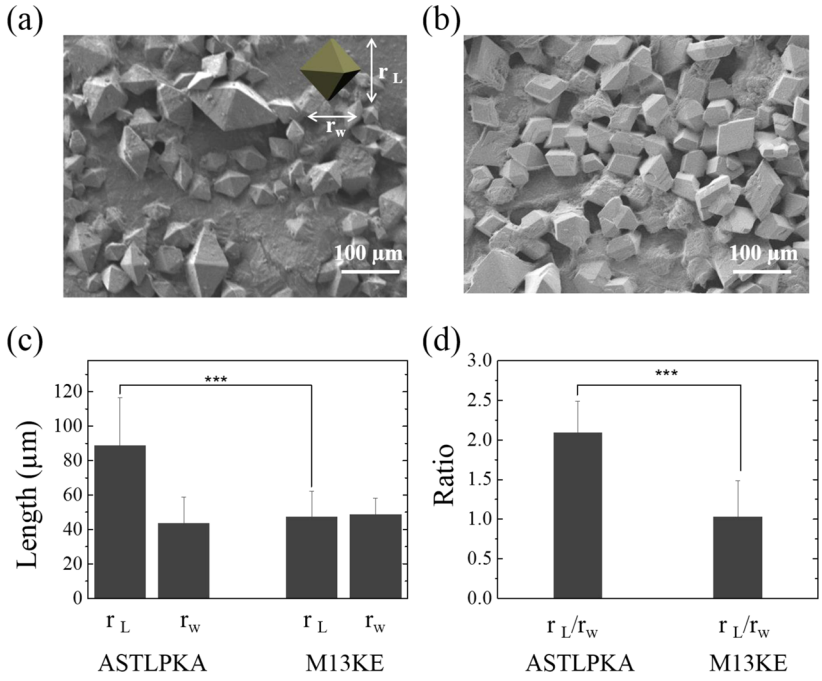

Figure 5. FE-SEM images of (tetragonal) bipyramidal TMX crystals obtained by cooling of a supersaturated TMX solution in the presence of (a) M13 bacteriophage expressing TMX-binding heptapeptide ASTLPKA and (b) wild-type M13KE and (c and d) the corresponding aspect ratios between the width and length of the tetragonal-bipyramidal shape, respectively (n = 20; Student t test; ***, $p < 0.001$).

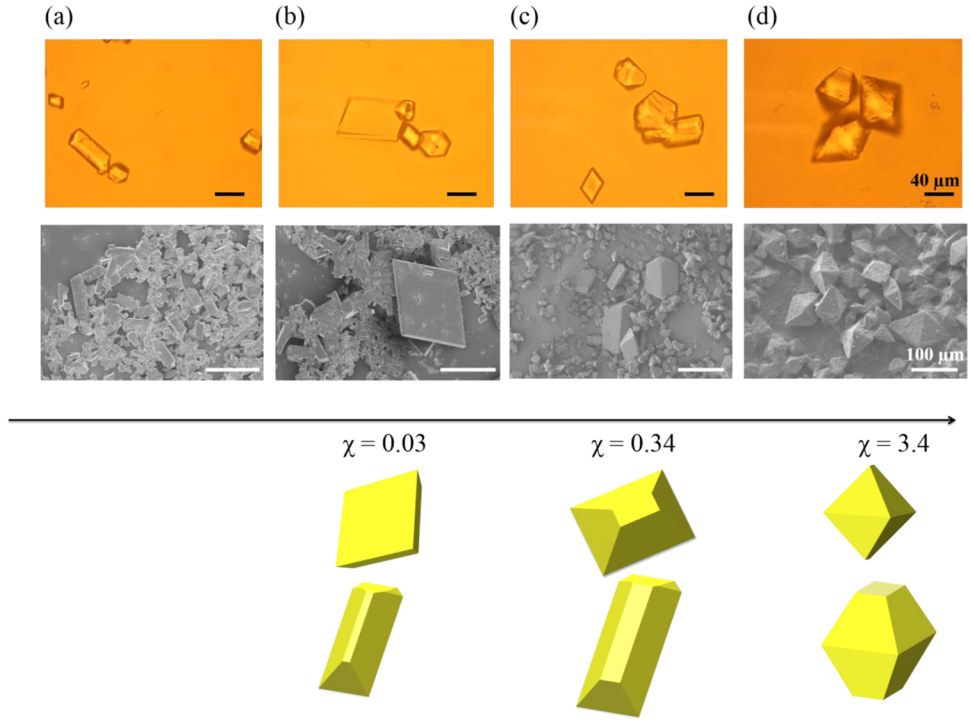

Figure 6. TMX crystal shape changes depending on $\chi = W_{phage}/W_{TMX}$: (a) no phage (control). Concentration of M13 bacteriophage expressing TMX-binding ASTLPKA is (b) 0.37 mg/mL (χ = 0.03), (c) 3.7 mg/mL (χ = 0.34), and (d) 37 mg/mL (χ = 3.4).

3.2. Phage Adsorption onto TMX Crystals. We hypothesize that the effectiveness of phage in facilitating the aggregation of irregular TMX primitive crystals into well-defined microstructures results from favorable interactions between phage and TMX as well as that of phage−phage interactions. In order to test our hypothesis, we carried out quantitative investigations to understand the characteristics of phage absorption behavior on the TMX crystal surface. We noted that the amount of phage adsorbed onto TMX increased and finally became saturated as the concentration of phage was increased up to 37 mg/mL ($\chi \sim 3.4$), as shown in Figure 7. The Langmuir equation is a physical adsorption model based on these three assumptions: monolayer coverage, adsorption site equivalence, and adsorption site independence. However, it led

DOI: 10.1021/acsami.5b05548
ACS Appl. Mater. Interfaces 2015, 7, 15707−15715

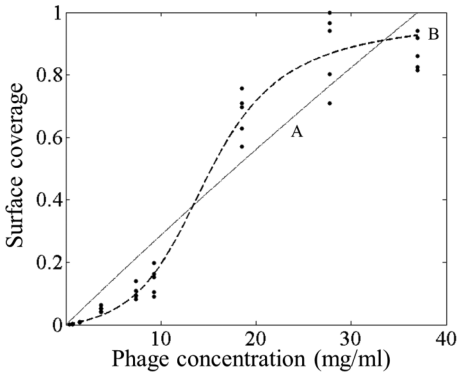

Figure 7. Comparison of model fitting to normalized phage adsorption isotherm onto TMX crystal surfaces in the solution environment. The solid line represents (A) a Langmuir adsorption model, and the dashed line represents (B) a Satake–Yang adsorption model.

to poor data fitting to the measured adsorption isotherm of phage on TMX (Figure 7, line A), apparently because it does not account for interactions between adsorption sites. Instead, the Satake–Yang model was used to fit the adsorption isotherm of phage onto TMX surfaces (Figure 7, curve B). The Satake–Yang model quantifies the extent of binding in terms of the binding constant (Ku) and the cooperativity parameter (u).[48] The curve was fitted to minimize the sum of the squared absolute error through an iterative improvement to those parameter values using the Levenberg–Marquardt algorithm.[57] The experimental data were well-fitted to the Satake–Yang model ($p \ll 0.01$ by the F test) with fitting parameters, $Ku = 6.53 \times 10^{-2} \pm 1.76 \times 10^{-3}$ $(\mathrm{mg/mL})^{-1}$ and $u = 12.93 \pm 1.87$. It can be inferred from this fit that the binding process is highly cooperative; i.e., additional phage prefers to bind next to previously bound phage rather than to a portion of TMX with no bound phage. The cooperativity (u) shows how many times greater is the probability to find ligands bound adjacent to each other than away from each other.[52] Therefore, it is about approximately 13 times more likely for phage to bind adjacent to each other than away from each other, implying a high chance of phage–phage interactions.[50]

4. CONCLUSIONS

In summary, we have demonstrated a new approach to controlling supersaturation for the growth of TMX with high morphological uniformity through filamentous M13 bacteriophage that has a high binding affinity to TMX crystals. We found that the TMX crystal morphology was sensitive to the phage concentration. In addition, it was demonstrated that phage-binding behavior was in reasonable agreement with the Satake–Yang adsorption model, which allows estimation of the TMX–phage binding parameter [$Ku = 6.53 \times 10^{-2} \pm 1.76 \times 10^{-3}$ $(\mathrm{mg/mL})^{-1}$] as well as the phage–phage cooperativity parameter ($u = 12.93 \pm 1.87$). We have presented a "proof of concept" investigation intended to establish the feasibility of using a combinatorial phage display library for the preparation of organic crystals with morphological uniformity. It adds to the diversity of phage concepts by using phage to modify the surface chemistry of organic crystals and control the crystal growth by manipulating the supersaturation profile with varied phage concentration and temperature. We expect that our findings here will be useful as a new route toward manipulation of the surface chemistry and controlled growth of organic crystalline APIs in both scientific studies and engineering applications. Specifically, future work could investigate peptide-based surfactants isolated from phages to specifically tailor crystal nucleation and growth. Such work would undoubtedly elucidate the possible mechanism of phage–phage interactions identified by the adsorption isotherm.

■ ASSOCIATED CONTENT

Supporting Information

X-ray crystallographic data in CIF format, optical image, FE-SEM image, XRD spectrum of TMX crystals, photographic images of TMX crystals obtained with different phage concentrations, simulated TMX crystal planes with Miller Indices, FE-SEM images of TMX crystals precipitated with saturated TMX solutions (37 mg/ml) as additives. The Supporting Information is available free of charge on the ACS Publications website at DOI: 10.1021/acsami.5b05548.

■ AUTHOR INFORMATION

Corresponding Author

*Tel: +1-302-831-0102. Fax: +1-302-831-1048. E-mail: furst@udel.edu.

Notes

The authors declare no competing financial interest.

■ ACKNOWLEDGMENTS

This work was financially supported by Syngenta Crop Protection. We thank Drs. Yoon Sung Nam, Zack Britton, and Anne S. Robinson for fruitful discussions on the mass production of phage, Dr. Dongyeon Cho for fruitful discussions on data analysis using the Levenberg–Marquardt algorithm, and Deborah Powell for FE-SEM measurement assistance at the Delaware Biotechnology Institute Bioimaging Center.

■ REFERENCES

(1) Burda, C.; Chen, X.; Narayanan, R.; El-Sayed, M. A. Chemistry and Properties of Nanocrystals of Different Shapes. *Chem. Rev.* **2005**, *105*, 1025–1102.

(2) Nokhodchi, A.; Bolourtchian, N.; Dinarvand, R. Crystal Modification of Phenytoin Using Different Solvents and Crystallization Conditions. *Int. J. Pharm.* **2003**, *250*, 85–97.

(3) Kubacka, A.; Fernandez-Garcia, M.; Colon, G. Advanced Nanoarchitectures for Solar Photocatalytic Applications. *Chem. Rev.* **2012**, *112*, 1555–1614.

(4) Qiu, X.; Leporatti, S.; Donath, E.; Möhwald, H. Studies on the Drug Release Properties of Polysaccharide Multilayers Encapsulated Ibuprofen Microparticles. *Langmuir* **2001**, *17*, 5375–5380.

(5) Graham, K. R.; Stalder, R.; Wieruszewski, P. M.; Patel, D. G.; Salazar, D. H.; Reynolds, J. R. Tailor-Made Additives for Morphology Control in Molecular Bulk-Heterojunction Photovoltaics. *ACS Appl. Mater. Interfaces* **2013**, *5*, 63–71.

(6) Zheng, X.; Kuang, Q.; Yan, K.; Qiu, Y.; Qiu, J.; Yang, S. Mesoporous TiO2 Single Crystals: Facile Shape-, Size-, and Phase-Controlled Growth and Efficient Photocatalytic Performance. *ACS Appl. Mater. Interfaces* **2013**, *5*, 11249–11257.

(7) Kreiner, M.; Moore, B. D.; Parker, M. C. Enzyme-Coated Micro-Crystals: A 1-step Method for High Activity Biocatalyst Preparation. *Chem. Commun.* **2001**, 1096–1097.

(8) Leem, G.; Sarangi, S.; Zhang, S.; Rusakova, I.; Brazdeikis, A.; Litvinov, D.; Lee, T. R. Surfactant-Controlled Size and Shape Evolution of Magnetic Nanoparticles. *Cryst. Growth Des.* **2009**, *9*, 32–34.

(9) Kowalczyk, B.; Bishop, K. J.; Lagzi, I.; Wang, D.; Wei, Y.; Han, S.; Grzybowski, B. A. Charged Nanoparticles as Supramolecular Surfactants for Controlling the Growth and Stability of Microcrystals. *Nat. Mater.* **2012**, *11*, 227–232.

DOI: 10.1021/acsami.5b05548
ACS Appl. Mater. Interfaces 2015, 7, 15707–15715

(10) Zhang, Y.; Sizemore, J. P.; Doherty, M. F. Shape Evolution of 3-Dimensional Faceted Crystals. *AIChE J.* **2006**, *52*, 1906−1915.
(11) Lovette, M. A.; Browning, A. R.; Griffin, D. W.; Sizemore, J. P.; Snyder, R. C.; Doherty, M. F. Crystal Shape Engineering. *Ind. Eng. Chem. Res.* **2008**, *47*, 9812−9833.
(12) Llinàs, A.; Goodman, J. M. Polymorph Control: Past, Present and Future. *Drug Discovery Today* **2008**, *13*, 198−210.
(13) Selloni, A. Crystal Growth: Anatase Shows Its Reactive Side. *Nat. Mater.* **2008**, *7*, 613−615.
(14) Uskoković, V.; Batarni, S. S.; Schweicher, J.; King, A.; Desai, T. A. Effect of Calcium Phosphate Particle Shape and Size on Their Antibacterial and Osteogenic Activity in the Delivery of Antibiotics In Vitro. *ACS Appl. Mater. Interfaces* **2013**, *5*, 2422−2431.
(15) Chen, S. A.; Xi, H. M.; Yu, L. Cross-Nucleation between ROY Polymorphs. *J. Am. Chem. Soc.* **2005**, *127*, 17439−17444.
(16) Desgranges, C.; Delhommelle, J. Insights into the Molecular Mechanism Underlying Polymorph Selection. *J. Am. Chem. Soc.* **2006**, *128*, 15104−15105.
(17) Diao, Y.; Helgeson, M. E.; Myerson, A. S.; Hatton, T. A.; Doyle, P. S.; Trout, B. L. Controlled Nucleation from Solution Using Polymer Microgels. *J. Am. Chem. Soc.* **2011**, *133*, 3756−3759.
(18) Eral, H. B.; López-Mejías, V.; O'Mahony, M.; Trout, B. L.; Myerson, A. S.; Doyle, P. S. Biocompatible Alginate Microgel Particles as Heteronucleants and Encapsulating Vehicles for Hydrophilic and Hydrophobic Drugs. *Cryst. Growth Des.* **2014**, *14*, 2073−2082.
(19) Geneviciute, L.; Florio, N.; Lee, S. Toward Polymorph Control in an Inorganic Crystal System by Templated Nucleation at a Microdroplet Liquid Interface: Potassium Hexacyanoferrate (II) Trihydrate. *Cryst. Growth Des.* **2011**, *11*, 4440−4448.
(20) Yin, J.; Zhou, J.; Sun, J.; Qiu, Y.; Wei, D.; Shen, Y. Study of the Crystal Shape and Its Influence on the Anti-tumor Activity of Tumor Necrosis Factor-Related Apoptosis-Inducing Ligand (Apo2L/TRAIL). *Cryst. Res. Technol.* **2008**, *43*, 888−893.
(21) Yang, H. G.; Sun, C. H.; Qiao, S. Z.; Zou, J.; Liu, G.; Smith, S. C.; Cheng, H. M.; Lu, G. Q. Anatase TiO2 Single Crystals with a Large Percentage of Reactive Facets. *Nature* **2008**, *453*, 638−641.
(22) Yang, G.; Kubota, N.; Sha, Z.; Louhi-Kultanen, M.; Wang, J. Crystal Shape Control by Manipulating Supersaturation in Batch Cooling Crystallization. *Cryst. Growth Des.* **2006**, *6*, 2799−2803.
(23) Brittain, H. G. *Polymorphism in Pharmaceutical Solids*; Informa Healthcare: London, 2009; Vol. *192*.
(24) Meldrum, F. C.; Cölfen, H. Controlling Mineral Morphologies and Structures in Biological and Synthetic Systems. *Chem. Rev.* **2008**, *108*, 4332−4432.
(25) Cantaert, B.; Kim, Y.; Ludwig, H.; Nudelman, F.; Sommerdijk, N. A.; Meldrum, F. C. Think Positive: Phase Separation Enables a Positively Charged Additive to Induce Dramatic Changes in Calcium Carbonate Morphology. *Adv. Funct. Mater.* **2012**, *22*, 907−915.
(26) Dickerson, M. B.; Sandhage, K. H.; Naik, R. R. Protein-and Peptide-Directed Syntheses of Inorganic Materials. *Chem. Rev.* **2008**, *108*, 4935−4978.
(27) Cha, J. N.; Shimizu, K.; Zhou, Y.; Christiansen, S. C.; Chmelka, B. F.; Stucky, G. D.; Morse, D. E. Silicatein Filaments and Subunits from a Marine Sponge Direct the Polymerization of Silica and Silicones In Vitro. *Proc. Natl. Acad. Sci. U. S. A.* **1999**, *96*, 361−365.
(28) Kisailus, D.; Truong, Q.; Amemiya, Y.; Weaver, J. C.; Morse, D. E. Self-Assembled Bifunctional Surface Mimics an Enzymatic and Templating Protein for the Synthesis of a Metal Oxide Semiconductor. *Proc. Natl. Acad. Sci. U. S. A.* **2006**, *103*, 5652−5657.
(29) Chen, C.; Rosi, N. L. Peptide-Based Methods for the Preparation of Nanostructured Inorganic Materials. *Angew. Chem., Int. Ed.* **2010**, *49*, 1924−1942.
(30) Brutchey, R. L.; Morse, D. E. Silicatein and the Translation of Its Molecular Mechanism of Biosilicification into Low Temperature Nanomaterial Synthesis. *Chem. Rev.* **2008**, *108*, 4915−4934.
(31) Orme, C.; Noy, A.; Wierzbicki, A.; McBride, M.; Grantham, M.; Teng, H.; Dove, P.; DeYoreo, J. Formation of Chiral Morphologies through Selective Binding of Amino Acids to Calcite Surface Steps. *Nature* **2001**, *411*, 775−779.
(32) de la Rica, R.; Matsui, H. Applications of Peptide and Protein-Based Materials in Bionanotechnology. *Chem. Soc. Rev.* **2010**, *39*, 3499−3509.
(33) Lee, S.; Gao, X.; Matsui, H. Biomimetic and Aggregation-Driven Crystallization Route for Room-Temperature Material Synthesis: Growth of β-Ga_2O_3 Nanoparticles on Peptide Assemblies as Nanoreactors. *J. Am. Chem. Soc.* **2007**, *129*, 2954−2958.
(34) Zhang, Z.; Gao, D.; Zhao, H.; Xie, C.; Guan, G.; Wang, D.; Yu, S. Biomimetic Assembly of Polypeptide-Stabilized $CaCO_3$ Nanoparticles. *J. Phys. Chem. B* **2006**, *110*, 8613−8618.
(35) Yoo, P. J.; Nam, K. T.; Qi, J.; Lee, S.; Park, J.; Belcher, A. M.; Hammond, P. T. Spontaneous Assembly of Viruses on Multilayered Polymer Surfaces. *Nat. Mater.* **2006**, *5*, 234−240.
(36) Mao, C.; Solis, D. J.; Reiss, B. D.; Kottmann, S. T.; Sweeney, R. Y.; Hayhurst, A.; Georgiou, G.; Iverson, B.; Belcher, A. M. Virus-Based Toolkit for the Directed Synthesis of Magnetic and Semiconducting Nanowires. *Science* **2004**, *303*, 213−217.
(37) Nam, K. T.; Kim, D. W.; Yoo, P. J.; Chiang, C. Y.; Meethong, N.; Hammond, P. T.; Chiang, Y. M.; Belcher, A. M. Virus-Enabled Synthesis and Assembly of Nanowires for Lithium Ion Battery Electrodes. *Science* **2006**, *312*, 885−888.
(38) Park, J. P.; Do, M.; Jin, H.; Lee, S.; Lee, H. M13 Bacteriophage Displaying DOPA on Surfaces: Fabrication of Various Nanostructured Inorganic Materials without Time-Consuming Screening Processes. *ACS Appl. Mater. Interfaces* **2014**, *6*, 18653−18660.
(39) Nam, Y. S.; Magyar, A. P.; Lee, D.; Kim, J.; Yun, D. S.; Park, H.; Pollom, T. S.; Weitz, D. A.; Belcher, A. M. Biologically Templated Photocatalytic Nanostructures for Sustained Light-Driven Water Oxidation. *Nat. Nanotechnol.* **2010**, *5*, 340−344.
(40) Miller, R. A.; Presley, A. D.; Francis, M. B. Self-Assembling Light-Harvesting Systems from Synthetically Modified Tobacco Mosaic Virus Coat Proteins. *J. Am. Chem. Soc.* **2007**, *129*, 3104−3109.
(41) Chung, W. J.; Oh, J.-W.; Kwak, K.-W.; Lee, B.-Y.; Meyer, J.; Wang, E.; Hexemer, A.; Lee, S.-W. Biomimetic Self-Templating Supramolecular Structures. *Nature* **2011**, *478*, 364−368.
(42) Lee, B.-Y.; Zhang, J.; Zueger, C.; Chung, W.-J.; Yoo, S.-Y.; Wang, E.; Meyer, J.; Ramesh, R.; Lee, S.-W. Virus-Based Piezoelectric Energy Generation. *Nat. Nanotechnol.* **2012**, *7*, 351−356.
(43) Oh, S.; Kwak, E.; Jeon, S.; Ahn, S.; Kim, J.; Jaworski, J. Responsive 3D Microstructures from Virus Building Blocks. *Adv. Mater.* **2014**, *26*, 5217−5222.
(44) Chopra, D.; Mohan, T. P.; Rao, K. S.; Row, T. N. G. CCDC 243116: Experimental Crystal Structure Determination, 2004.
(45) Cölfen, H.; Antonietti, M. Mesocrystals: Inorganic Superstructures Made by Highly Parallel Crystallization and Controlled Alignment. *Angew. Chem., Int. Ed.* **2005**, *44*, 5576−5591.
(46) Cho, W.; Fowler, J. D.; Furst, E. M. Targeted Binding of the M13 Bacteriophage to Thiamethoxam Organic Crystals. *Langmuir* **2012**, *28*, 6013−6020.
(47) Satake, I.; Yang, J. T. Interaction of Sodium Decyl Sulfate with Poly (L-ornithine) and Poly (L-lysine) in Aqueous Solution. *Biopolymers* **1976**, *15*, 2263−2275.
(48) Nishio, T.; Shimizu, T.; Kwak, J. C. T.; Minakata, A. The Cooperative Binding of Large Ligands to a One-Dimensional Lattice: The Steric Hindrance Effect. *Biophys. Chem.* **2003**, *104*, 501−508.
(49) Lapitsky, Y.; Parikh, M.; Kaler, E. W. Calorimetric Determination of Surfactant/Polyelectrolyte Binding Isotherms. *J. Phys. Chem. B* **2007**, *111*, 8379−8387.
(50) Li, D.; Kelkar, M. S.; Wagner, N. J. Phase Behavior and Molecular Thermodynamics of Coacervation in Oppositely Charged Polyelectrolyte/Surfactant Systems: A Cationic Polymer JR 400 and Anionic Surfactant SDS Mixture. *Langmuir* **2012**, *28*, 10348−10362.
(51) Li, D.; Wagner, N. J. Universal Binding Behavior for Ionic Alkyl Surfactants with Oppositely Charged Polyelectrolytes. *J. Am. Chem. Soc.* **2013**, *135*, 17547−17555.
(52) Schwarz, G. Cooperative Binding to Linear Biopolymers. *Eur. J. Biochem.* **1970**, *12*, 442−453.
(53) Matulis, D.; Rouzina, I.; Bloomfield, V. A. Thermodynamics of Cationic Lipid Binding to DNA and DNA Condensation: Roles of

DOI: 10.1021/acsami.5b05548
ACS Appl. Mater. Interfaces 2015, 7, 15707−15715

Electrostatics and Hydrophobicity. *J. Am. Chem. Soc.* **2002**, *124*, 7331−7342.
(54) Jaworski, J. W.; Raorane, D.; Huh, J. H.; Majumdar, A.; Lee, S.-W. Evolutionary Screening of Biomimetic Coatings for Selective Detection of Explosives. *Langmuir* **2008**, *24*, 4938−4943.
(55) Song, R.; Cölfen, H. Mesocrystals—Ordered Nanoparticle Superstructures. *Adv. Mater.* **2010**, *22*, 1301−1330.
(56) Wang, Y.; Kim, Y.; Christenson, H. K.; Meldrum, F. C. A New Precipitation Pathway for Calcium Sulfate Dihydrate (Gypsum) via Amorphous and Hemihydrate Intermediates. *Chem. Commun.* **2012**, *48*, 504−506.
(57) Marquardt, D. W. An Algorithm for Least-Squares Estimation of Nonlinear Parameters. *J. Soc. Ind. Appl. Math.* **1963**, *11*, 431−441.

DOI: 10.1021/acsami.5b05548
ACS Appl. Mater. Interfaces 2015, 7, 15707−15715